Accepted Manuscript

Ionic and electronic transport in calcium-substituted LaAlO₃ perovskites prepared via mechanochemical route

Martin Fabián[1*], Blanca I. Arias-Serrano[2], Aleksey A. Yaremchenko[2*], Hristo Kolev[3,4], Mária Kaňuchová[4], Jaroslav Briančin[1]

[1] Institute of Geotechnics, Slovak Academy of the Sciences, Watsonova 45, 0401Košice, Slovakia

[2] CICECO – Aveiro Institute of Materials, Department of Materials and Ceramic Engineering, University of Aveiro, 3810-193 Aveiro, Portugal

[3] Institute of Catalysis, Bulgarian Academy of Sciences, Acad. G. Bonchev St., Bldg. 11, 1113 Sofia, Bulgaria

[4] Technical University of Košice, Letná 9, 04200 Košice, Slovakia

*corresponding authors: Martin Fabián, fabianm@saske.sk; Aleksey A. Yaremchenko, ayaremchenko@ua.pt

Abstract

The present work explores mechanosynthesis of lanthanum aluminate-based perovskite ceramics and corresponding effects on ionic-electronic transport properties. $La_{1-x}Ca_xAlO_{3-\delta}$ ($x = 0.05$-0.20) nanopowders were prepared *via* one-step high-energy mechanochemical processing. Sintering at 1450°C yielded dense ceramics with submicron grains. As-prepared powders and sintered ceramics were characterized by XRPD, XPS and SEM. Electrochemical studies showed that partial oxygen-ionic conductivity in prepared $La_{1-x}Ca_xAlO_{3-\delta}$ increases with calcium content up to 10 at.% in the lanthanum sublattice and then levels off at $\sim 6 \times 10^{-3}$ S/cm at 900°C. $La_{1-x}Ca_xAlO_{3-\delta}$ ceramics are mixed conductors under oxidizing conditions and ionic conductors with negligible contribution of electronic transport in reducing atmospheres. Oxygen-ionic contribution to the total conductivity is 20-68% at 900°C in air and increases with Ca content, with temperature and with reducing $p(O_2)$. Impedance spectroscopy results showed however that electrical properties of mechanosynthesized $La_{1-x}Ca_xAlO_{3-\delta}$ ceramics below ~ 800°C are determined by prevailing grain boundary contribution to the total resistivity.

Keywords: Lanthanum aluminate, Mechanosynthesis, Perovskite, Conductivity, Solid electrolyte

1. Introduction

Lanthanum aluminate $LaAlO_3$ with perovskite-like structure is a semiconductor with a low electrical conductivity, $< 5 \times 10^{-4}$ S/cm at 900°C in air [1-4]. Acceptor-type doping of $LaAlO_3$ and related $LnAlO_3$ perovskites was found to increase the concentration of oxygen vacancies in the perovskite-lattice and, consequently, to induce oxygen-ionic conductivity [2,5-8]. This attracted attention to $LaAlO_3$-based oxides as potential candidates for electrolytes of

solid oxide fuel cells [3,4,9-13]. The substitutions of lanthanum by alkaline-earth elements (A = Ca, Sr, Ba) [2-4,9,10] or aluminum by magnesium [4,8,10] as well as simultaneous co-substitutions into both sublattices [4,10-12] have been demonstrated to result in increase of ionic transport by orders of magnitude if compared to the parent lanthanum aluminate. $(La,A)(Al,Mg)O_{3-\delta}$ ceramics were reported to exhibit noticeable contribution of p-type electronic transport under oxidizing conditions, but nearly pure ionic conduction under reduced oxygen chemical potentials [8-13]. Enhancement of the ionic conductivity was also achieved via co-doping by Ba and Y into La and Al sublattices, respectively [1], while the substitution of aluminum by manganese in $(La,Sr)AlO_{3-\delta}$ results in an increase of electronic transport [3,14,15]. Villas-Boas and de Souza [16] reported a positive effect of Pr co-doping on the electrical transport properties of Sr-substituted $LaAlO_3$, mainly by suppressing the grain boundary resistivity.

Despite the ionic conductivity of $LaAlO_3$-based perovskites is relatively low, these materials exhibit certain advantages. Those include a better stability with respect to reduction and components volatilization under reducing atmospheres if compared to CeO_2-, $LaGaO_3$- and silicate-based materials [17]. Taking into account the comparatively low cost, ionic conductors derived from $LaAlO_3$ are still of potential interest, particularly for the anode protective layers and as additives to composite solid electrolytes [17-19].

There are a number of works describing different approaches to the synthesis of $LaAlO_3$ including conventional solid state reaction route [6-9,12,20,21], solvothermal [22], combustion [23-26], reverse micelle [27], in situ polymerization [28], molten salt [29,30], precipitation [31], electrochemical [32] and mechanochemical [33] methods. The latter approach is of particular interest being a low-temperature, high-reproducibility, solvent-free and relatively low-cost method of synthesis of nanostructured complex oxides [34].

In this context, the primary objective of this paper is to introduce a new preparation method of Ca-substituted $LaAlO_3$ nanoparticles via a mechanochemical route. Atomistic simulation study of $LaGaO_3$ counterpart demonstrated a strong preference of Ca cations for lanthanum sites in the perovskite lattice [35]. The mechanism of substitution by Ca^{2+} for La^{3+} in $LaAlO_3$ and generation of oxygen vacancies is given by equation (using Kröger–Vink notation):

$$0.5(1-x)La_2O_3 + xCaO + 0.5Al_2O_3 \rightarrow (1-x)La_{La}^{\times} + xCa_{La}' + Al_{Al}^{\times} + (3-0.5x)O_O^{\times} + 0.5xV_O^{\cdot\cdot} \qquad (1)$$
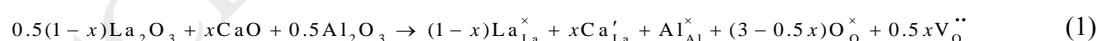
The data on the solid solubility of calcium in lanthanum aluminate is not available, however, the Ca solubility limit was reported to be close to 10 at.% in A sublattice in the case of $Nd_{1-x}Ca_xAlO_{3-\delta}$ analogues [6].

Although the mechanosynthesis of undoped $LaAlO_3$ has already been reported by Zhang and Saito [33], it should be noted that the formation of desired compound has been achieved after relatively long time of ball milling. Moreover, in our present study we provide rapid mechanosynthesis and detailed structural study on as-prepared and subsequently sintered Ca-substituted $LaAlO_3$ utilizing X-ray powder diffraction (XRPD) and X-ray photoelectron spectroscopy (XPS). Accordingly, it is shown that the simultaneous use of diffraction techniques, which are sensitive to medium- and

long-range structural order, and spectroscopic techniques, which make possible observations on a local atomic scale, is often necessary to allow a comprehensive characterization of the product of chemical reactions. Structural, microstructural and spectroscopic studies were complemented by the detailed electrical characterization of mechanosynthesized $La_{1-x}Ca_xAlO_{3-\delta}$ ceramics in a broad range of temperatures and oxygen partial pressures, including the determination of grain bulk and grain boundary contributions to the total electrical conductivity as well as partial ionic and electronic conductivities at 600-900°C.

2. Experimental

Ca-substituted $LaAlO_3$ powders were prepared by mechanochemical method. Solid precursors, lanthanum oxide (La_2O_3, 99.9 % purity, Aldrich), aluminum oxide (γ-Al_2O_3, 99.9 % purity, Aldrich) and calcium oxide (CaO, 99.9 % purity, Aldrich) were used for the mechanosynthesis. For each composition, a mixture (5 g) of precursors taken in appropriate proportions was milled for various times (up to 30 min) in a high-energy planetary ball mill Pulverisette 6 (Fritsch, Germany). A grinding chamber (200 cm^3 in volume) and balls (10 mm in diameter) made of tungsten carbide were used. The ball-to-powder weight ratio was 40:1. Milling experiments were performed in an ambient atmosphere at 600 rpm. The as-prepared powders were pressed into several disks of 16 mm diameter and 2 mm thickness at 270MPa. Polyetheylene glycol (PEG) 10 000 was used as a plasticizer. The pellets were sintered at 1450°C for 12 h in air (except $LaAlO_3$ sintered at 1700°C).

The crystal structure of as-prepared powders and sintered samples was investigated by XRPD. The XRPD patterns were collected using a D8 Advance diffractometer (Brucker, Germany) with the CuKα radiation in the Bragg-Brentano configuration. The generator was set up at 40 kV and 40 mA. The divergence and receiving slits were 0.3° and 0.1 mm, respectively. The XRPD patterns were recorded in the range 2Θ = 20–72° with a step of 0.03° and a measuring time of 20 s. Due to the presence of contaminations and amorphous phase, the refinements were performed using Le Bail method (refinement without structural constraints [36]). Le Bail analyses of XRPD data of the as-prepared and sintered samples were performed in the space group *Pm-3m* using Fullprof computer program [37]. The XRPD line broadening was analyzed by the refinement of regular Thompson-Cox-Hastings pseudo-Voigt function parameters [38]. In order to obtain proper geometry set-up and to eliminate instrumental broadening, the instrumental resolution function was determined by refinement of LaB_6 standard specimen. The JCPDS PDF database was utilized for the phase identification [39].

XPS measurements have been carried out on the ESCALAB MkII (VG Scientific) electron spectrometer at a base pressure in the analysis chamber of 5×10^{-10} mbar (2×10^{-9} mbar during the measurement) using twin non-monochromatic anode MgKα/AlKα X-ray source with excitation energies of 1253.6 and 1486.6 eV, respectively. Passing through a 6-mm slit (entrance/exit) of a hemispherical analyzer, electrons with pass energy of 20 eV are

detected by a channeltron. The spectra were recorded at the total instrumental resolution (as it was measured with the FWHM of Ag3d$_{5/2}$ photoelectron line) of 1.06 and 1.18 eV for MgKα and AlKα excitation sources, respectively. The energy scale has been calibrated by normalizing the C1s line of adsorbed adventitious hydrocarbons to 285.0 eV. The processing of the measured spectra includes a subtraction of X-ray satellites and Shirley-type background [40]. The peak positions and areas are evaluated by a symmetrical Gaussian-Lorentzian curve fitting. The relative concentrations of the different chemical species are determined based on normalization of the peak areas to their photoionization cross-sections, calculated by Scofield [41].

The morphology of La$_{1-x}$Ca$_x$AlO$_{3-\delta}$ powders and sintered pellets were observed using the high resolution scanning electron microscopy (FE-SEM) (Mira III, Tescan, Czech Republic). ImageJ software [42] was used to evaluate FE-SEM micrographs. The Energy-dispersive X-ray spectroscopy (EDX) detector (Oxford Instruments, UK) was used to determine the elemental composition of the final products.

Total electrical conductivity (σ) was determined by impedance spectroscopy (Agilent 4284A precision LCR meter) using ceramic samples with applied porous Pt electrodes. The measurements were performed as function of temperature in air at 340-1000°C and as function of oxygen partial pressure at 600-1000°C using flowing O$_2$+N$_2$ and 10%(H$_2$+H$_2$O)+90%N$_2$ gas mixtures. Bronkhorst mass-flow controllers were used to mix the gases. Oxygen partial pressure, p(O$_2$), in a gas flow was continuously monitored using yttria-stabilized zirconia oxygen sensor. The average ion transference numbers under air/O$_2$ and air/(10%H$_2$+90%N$_2$) gradients were determined at 700-900°C by the modified electromotive force (EMF) technique taking electrode polarization into account [43-45].

3. Results and discussion

The formation of LaAlO$_3$ in the course of mechanosynthesis was followed by XRPD. As it is exemplarily shown in Fig. 1a, the XRPD pattern of the starting (unmilled) mixture is characterized by sharp diffraction peaks corresponding to La$_2$O$_3$ and La(OH)$_3$. The formation of La(OH)$_3$ can be explained by hygroscopic character of lanthanum oxide. The XRPD peaks corresponding to γ-Al$_2$O$_3$ are not visible due to its amorphous nature [46]. After 3 min of intensive ball milling, the Bragg reflections decrease in intensity and broadened. On the other hand, new Bragg reflections belonging to LaAlO$_3$ are formed. After 30 min of milling, all the diffraction peaks can be attributed to the LaAlO$_3$ only (S.G. *Pm-3m*). XRPD patterns of mechanosynthesized La$_{1-x}$Ca$_x$AlO$_{3-\delta}$ ($0 \leq x \leq 0.2$) solid solutions are shown in Fig. 1b. The effective incorporation of calcium into the perovskite-type structure of LaAlO$_3$ results in slight shift of all characteristic XRPD reflections to the higher angular positions (lower values of d-spacing), indicating a lattice contraction of La$_{1-x}$Ca$_x$AlO$_{3-\delta}$ with increasing Ca^{2+} content. XRPD patterns of La$_{1-x}$Ca$_x$AlO$_{3-\delta}$ ($0 \leq x \leq 0.2$) sintered at 1450°C in air are shown in Fig. 1c. In addition to the main perovskite phase, XRPD pattern of undoped LaAlO$_3$ showed the presence of considerable fraction of secondary LaAl$_{11}$O$_{18}$ (hexagonal S.G. *P6$_3$/mmc*) phase.

4

Increasing sintering temperature to 1700°C did not help to improve the phase purity of this material. Incorporation of Ca resulted in reduction of secondary phase content. Within the XRPD detection limit no impurity phases containing Ca, as possible by-products of the sintering process, have been observed.

Fig. 1

As it is listed in Table 1, the lattice parameters of the mechanosynthesized materials vary with calcium content. Unit cell volume shrinkage of $La_{1-x}Ca_xAlO_{3-\delta}$ solid solutions compared to calcium-free $LaAlO_3$ is the consequence of incorporation of Ca cations into La sites and increase in oxygen vacancy concentration in the perovskite lattice of $LaAlO_3$. On top of that, it was found that the crystallite size increased when calcium is introduced into the structure (Table 1). However, for calcium-containing compositions, increasing calcium concentration influenced the crystallite size rather negligibly. On the other hand, the accumulated microstrain changed significantly once calcium is introduced in the structure of perovskite. This is obvious if we consider that cations replacement and generation of oxygen defects is accompanied by changes in the geometry of the structural units of the material. This alteration is evident if we take into consideration slightly different ionic radii of La^{3+} and Ca^{2+} ions in their twelve-coordinated positions; $r(La^{3+})_{XII}$ = 1.36 Å / $r(Ca^{2+})_{XII}$ = 1.34 Å [47].

Table 1

In addition, the lattice parameters of the mechanosynthesized materials were found to be larger in comparison to the sintered samples (Table 1), with typical values for $LaAlO_3$ as reported elsewhere [48]. The disappearance observed for the lattice shrinkage with applied thermal treatment can be ascribed to the structural relaxation of the samples [49]. In order to obtain information related to the local structure modification, the as-sintered samples were crushed, refined and investigated by XPS. Fig. 2a shows the high resolution XPS spectra of La $3d_{5/2}$ and its satellite for $LaAlO_3$ and $La_{0.8}Ca_{0.2}AlO_{3-\delta}$ ceramics after sintering. The binding energies in the range of 834.1–834.5 eV are typical for La^{3+}. The differences of 0.4 eV between $La3d_{5/2}$ states in both samples can be explained by presence of Ca in $La_{0.8}Ca_{0.2}AlO_{3-\delta}$ sample, which assure different surrounding of La atoms and thus change in the binding energy. The satellite peak has 3.8 eV higher binding energy. This can be attributed to the La-OH bonds [50] due to the hygroscopic character of lanthanum based oxides. Quantitative analysis of XPS spectra revealed the La-O/La-OH bonds ratio 23/77 for $LaAlO_3$ and 21/79 for $La_{0.8}Ca_{0.2}AlO_{3-\delta}$, respectively. Fig. 2b displays Al2p core level of $LaAlO_3$ and $La_{0.8}Ca_{0.2}AlO_{3-\delta}$. Binding energy of 74.4 eV is typical for Al^{3+} state representing Al-O and/or Al-OH bonds. However, for calcium containing sample, the Al 2p level shifts to the lower binding energy and peak becomes asymmetric. Two peaks can be derived from this spectrum: The higher binding energy located at 74.0 eV is ascribed to Al^{3+}; the lower binding energy located at 72.9 eV could be assigned to the different surrounding of Al ions as oxygen vacancies are formed. Accordingly, the chemical state refers to the local bonding environment of Al ions. The local bonding environment is affected by its oxidation state, the identity of its nearest-neighbor atom or lack of it, its bonding hybridization to that nearest-neighbor

atom, which applied a crystal field on the element. This field creates an extra pressure on the element so the binding energy required to ejection of electron is slight modified.

Fig. 2c shows the Ca2p spectra of $La_{0.8}Ca_{0.2}AlO_{3-\delta}$ compared with Ca2p core level of standard spectra measured for CaO and $CaCO_3$. Binding energy of the $2p_{3/2}$ peak (BE$2p_{3/2}$) and difference between BE$2p_{3/2}$ and binding energy of core level satellite Δ = BE$2p_{3/2}$-BEsat were compared. BE of Ca$2p_{3/2}$ measured for $La_{0.8}Ca_{0.2}AlO_{3-\delta}$ is 346.9 eV, whereas Δ=8.6 eV. These values are between the values extracted from the standard spectra of CaO and $CaTiO_3$. The XPS parameters were found to be BE$2p_{3/2}$ = 347.6 eV and $\Delta \sim 8$ eV for octahedrally coordinated Ca in CaO and BE$2p_{3/2}$ = 346.8 eV and $\Delta \sim 9$ eV for twelve coordinated Ca in $CaTiO_3$. Comparison of those values indicates that the Ca$2p_{3/2}$ peak measured for $La_{0.8}Ca_{0.2}AlO_{3-\delta}$ ceramics consists of subpeaks with binding energy values between six-fold and twelve-fold coordinated positions of Ca. Again, the shift in binding energy most likely originates from different surrounding of Ca ions due to the decrease in coordination number as oxygen vacancies are introduced. Although Sood et $al.$ [51] reported on partial Ca^{2+} occupation at B site in $LaInO_3$, the Ca^{2+} – Al^{3+} replacement is considered to be negligible due to the significant difference between ionic radii of Ca^{2+} and Al^{3+} ions in their octahedrally coordinated positions; $r(Al^{3+})_{VI}$ = 0.535 Å / $r(Ca^{2+})_{VI}$ = 1.00 Å [47]. However, more precise study should be done to shed light on proper structure explanation in Ca-doped LaMO_3 (M = Al, Ga, In) perovskite systems.

Fig. 2

The study of the microstructure was carried out to estimate the density, shape and size of the grains (Figs. 3a–3d). The density of sintered pellets determined by Archimedes method exceed 95 % of theoretical values (Table 1), except for undoped $LaAlO_3$ ceramics which still had relative density of only 63% even after sintering at 1700°C.

The results of morphological analysis show that the grain size and shape of sintered samples is affected by calcium doping. For $LaAlO_3$ (Fig. 3a), the non-uniform grains with noticeable porosity are observed, which is in agreement with lower density of these samples. The nucleation of the hexagonal $LaAl_{11}O_{18}$ phase can be seen in some parts of the structure. However, due to the small volume fraction of the secondary phase and since there is not much difference in grain size, it is difficult to visualize the structure as observed in XRPD pattern. The average grain size of $LaAlO_3$ was found to be 1.18 μm (Table 1). As shown in Figs. 3 (b–d) the average grain size in the samples containing calcium is reduced bellow 1 μm. Accordingly, the Ca-doping hinders the grain growth of the parent perovskite phase $LaAlO_3$. As the dopant concentration increases, a refined structure consisting of small grains with a narrow distribution is obtained. The EDX analysis, to a great extent, confirms homogeneity of the prepared materials (Fig. 3e). As listed in Table 2, the average elemental composition for homogenous regions of the samples is very close to the nominal composition.

Fig. 3

Table 2

The results of electrical measurements showed that undoped $LaAlO_3$ is an insulator with electrical conductivity as low as 3.4×10^{-5} S/cm at 900°C in air (Fig. 4) and corresponding activation energy of 148 kJ/mol (Table 3). These observations are generally in agreement with the literature data, although the reported conductivity values scatter in a wide range from 1.1×10^{-6} to 1.4×10^{-3} S/cm at 900°C in air [1-4,10]; this implies a strong influence of the phase and elemental impurities, porosity and microstructural characteristics.

Table 3

Acceptor-type substitution of lanthanum by calcium results in a 2-3 orders of magnitude increase of the total electrical conductivity in the high-temperature range (Fig. 4) and a decrease in activation energy of conductivity (Table 3). At the same time, increasing calcium content above 10 at.% in the lanthanum sublattice has rather negligible effect: the level of total conductivity is nearly independent of calcium content for the composition with $x = 0.10\text{-}0.20$ at temperature above ~550°C (Figs. 4 and 5).

Fig. 4.

Fig. 5.

Impedance spectroscopy studies revealed a strong contribution of grain boundary resistivity to the total resistivity of $La_{1-x}Ca_xAlO_{3-\delta}$ ceramics. As an example, Fig. 6 shows impedance spectra of $x = 0.15$ ceramic sample recorded at different temperatures in air. Three different contributions are clearly observed in the studied frequency range. Low-frequency contribution visible only at higher temperatures was attributed to the electrode process. Intermediate-frequency arc (specific capacitance $\sim2\times10^{-9}$ F/cm) and high-frequency semicircle ($\sim2\times10^{-11}$ F/cm, visible only at lower temperatures in the studied frequency range) were assigned to the grain boundary and the grain bulk contributions to the total resistivity, respectively. The spectra were fitted using a simple $(R_{HF}//CPE_{HF})(R_{IF}//CPE_{IF})CPE_{LF}$ equivalent circuit to extract the bulk and grain boundary resistivities.

Fig. 6.

Analysis of the impedance spectroscopy data showed that electrical properties of mechanosynthesized $La_{1-x}Ca_xAlO_{3-\delta}$ ceramics at temperatures below ~800°C are dominated by the grain boundary resistivity (Fig. 7a). Grain boundary-limited electrical conduction in the low-temperature range was reported earlier for Sr- and Mg- co-substituted $La_{0.9}Sr_{0.1}Al_{0.9}Mg_{0.1}O_{3-\delta}$ ceramics [12]. The grain boundary conductivity has a higher activation energy compared to the bulk conductivity, and the extrapolation indicates that the total conductivity is limited by the grain boundary conductivity in the low-temperature range and by the bulk conductivity in the high-temperature range (Fig. 7a). Fig. 7b compares the bulk conductivities of $La_{1-x}Ca_xAlO_{3-\delta}$ ceramics at 330-680°C. As for the total conductivity, the bulk conductivity in this temperature range increases slightly with increasing calcium content from 5 to 10 at.% in the A sublattice, and is essentially composition-independent for $x \geq 0.10$.

Fig. 7.

7

Fig. 8(a and b) shows the results of measurements of total electrical conductivity as function of oxygen partial pressure. As for other acceptor-doped LaAlO₃-based materials [6,9-12,21], electrical conductivity of mechanosynthesized $La_{1-x}Ca_xAlO_{3-\delta}$ ceramics decreases with reducing $p(O_2)$ under oxidizing conditions, in the $p(O_2)$ range between 10^{-5} and 1.0 atm, and show a plateau-like behavior under reducing conditions when $p(O_2)$ is below $\sim 10^{-10}$ atm. The changes in electrical conductivity with oxygen partial pressure can be understood considering the defect chemistry of acceptor-doped LaAlO₃. Incorporation of oxygen into the perovskite lattice on increasing $p(O_2)$ is accompanied by generation of electron-holes and is expressed by equation:

$$V_O^{\bullet\bullet} + 0.5O_2 \xleftrightarrow{K_{ox}} O_O^{\times} + 2h^{\bullet} \tag{2}$$

with corresponding equilibrium constant

$$K_{ox} = \frac{[O_O^{\times}]}{[V_O^{\bullet\bullet}]}\frac{[h^{\bullet}]^2}{p(O_2)^{1/2}} = \frac{3-\delta}{\delta}\frac{p^2}{p(O_2)^{1/2}} \tag{3}$$

where p is the concentration of electron-holes. The concentrations of point defects are interrelated by electroneutrality conditions:

$$[Ca_{La}'] = 2[V_O^{\bullet\bullet}] + [h^{\bullet}] \qquad \text{or} \qquad x = 2\delta + p \tag{4}$$

Combining eqn.(3) with the definition of partial electrical conductivity, one obtains the expression for the p-type electronic conductivity which increases with increasing oxygen partial pressure:

$$\sigma_p = e\mu_p \ p = e\mu_p \ K_{ox}^{1/2}\left(\frac{3-\delta}{\delta}\right)^2 p(O_2)^{1/4} \tag{5}$$

where μ_p is the electron-hole mobility. Under reducing conditions, when the concentration of electron-holes is negligible, the electroneutrality condition can be simplified to

$$[Ca_{La}'] = 2[V_O^{\bullet\bullet}] \qquad \text{or} \qquad x = 2\delta \tag{6}$$

i.e., the concentration of oxygen vacancies is fixed by the doping level, and $p(O_2)$-independent oxygen-ionic conductivity σ_O dominates under reducing conditions. Assuming that the variations of oxygen content are negligible in the entire $p(O_2)$ range and the mobility of charge carriers are essentially independent of the defect concentrations, total electrical conductivity can be expressed by a simplified model:

$$\sigma_{total} = \sigma_O + \sigma_p = \sigma_O + \sigma_p^0 \ p(O_2)^{1/4} \tag{7}$$

where σ_p^0 is electron-hole conductivity at $p(O_2) = 1$ atm. By fitting the experimental data to eqn.(7), one may separate ionic and electronic contributions to the total electrical conductivity (Fig. 8c).

Fig. 8.

Fig. 9 compares the values of partial ionic and p-type electronic conductivities in air obtained by fitting the $\sigma - p(O_2)$ data (Fig. 8(a and b)). Increasing calcium content from 5 to 10 at.% in the lanthanum sublattice results in almost 5-fold increase of ionic conductivity, while further calcium doping leads to rather negligible improvement of ionic transport. At the same time, electron-hole conductivity has a tendency to decrease with increasing calcium content.

Fig. 9.

All studied $La_{1-x}Ca_xAlO_{3-\delta}$ ceramics are mixed ionic-electronic conductors under oxidizing conditions (Fig. 10). Electronic transport dominates in the $x = 0.05$ ceramics, with ionic contribution of only 20% to the total conductivity at 900°C in air. Oxygen-ion transference numbers t_O increase with calcium content and vary in the range 0.52-0.68 for other compositions under these conditions (Fig. 10). Analysis of the data showed also that the p-type electronic conductivity has a lower activation energy compared to the oxygen-ionic conductivity (Fig. 9b). As a result, the contribution of ionic transport to the total conductivity in air increases with increasing temperature (at least, for $x = 0.15$). Under reducing conditions, all $La_{1-x}Ca_xAlO_{3-\delta}$ ceramics are pure ionic conductors (Fig. 10).

Fig. 10.

The results of analysis of $\sigma - p(O_2)$ dependencies are in excellent agreement with the values of average oxygen-ionic transference numbers $\overline{t_O}$ obtained by the modified EMF technique under air/O$_2$ and air/(10% H$_2$-N$_2$) gradients (Table 4). These data confirm that ionic contribution to the total conductivity increases with increasing calcium content and with reducing oxygen partial pressure. Measured $\overline{t_O}$ values tend to increase with increasing temperature, in conformity with the higher activation energy for the oxygen-ionic conductivity (Fig. 9b). In the case of $x = 0.20$, average ionic transference number are close to unity under large p(O$_2$) gradients at 700-900°C.

Table 4

Overall, the obtained results demonstrate that the substitution by calcium results in an increase of ionic conductivity up to $x = 0.10$. Further calcium additions are favorable for the suppression of electronic contribution to the total electrical transport, but have rather minor impact on the absolute values of ionic conductivity, contrary to expectations based on eqn.(6). This, however, can be explained if one assumes a limited solubility of calcium in lanthanum sublattice close to ~10 at.% or slightly higher. Small amounts of secondary phases often cannot be detected by XRD analysis. For instance, Kilner et al. [5] studied $La_{1-x}Ca_xAlO_{3-\delta}$ ($x \leq 0.10$) and other lanthanum aluminate-based ceramics and detected the presence of secondary phase in all prepared materials by optical and electron microscopy, whereas XRD analysis showed that the samples are phase-pure. Ishihara et al. [6] reported that the solubility limit of calcium in neodymium sublattice of NdAlO$_3$ is somewhat below 10 at.%, while the dependence of total electrical conductivity of $Nd_{1-x}Ca_xAlO_{3-\delta}$ ($x = 0.05–0.30$) ceramics resembles that observed in the present work for $La_{1-x}Ca_xAlO_{3-\delta}$ system. In the present work, microstructural studies by FE-SEM/EDX did not detect the impurity phases but, due to the

small grain sizes (Fig. 3 and Table 1) and limitations of the technique, cannot exclude their segregation at the grain boundaries.

Another explanation was proposed by Nguyen et al. [10]. In particular, they reported that the solubility limit of strontium in the lanthanum sublattice of $La_{1-x}Sr_xAlO_{3-\delta}$ corresponds to ~20 at.%. At the same time, it was observed that the ionic conductivity in these series increases with increasing strontium content and, therefore, oxygen vacancy concentration up to $x = 0.10$, and then declines on further strontium doping. This was explained by the concentration-dependent mobility of oxygen vacancies. The drop in mobility for the compositions with $x > 0.1$ was discussed in terms of possible point defect association, e.g. $\{Sr'_{La} V_O^{\cdot\cdot}\}$, and trapping of oxygen vacancies responsible for the ionic conduction. Same considerations may be applicable in the case of $La_{1-x}Ca_xAlO_{3-\delta}$ system studied in the present work. One should point, however, that the conclusions on the solubility limits in Ref.[10] have been done based on the XRD data only.

Fig. 11 compares oxygen-ionic conductivity of $x = 0.15$ ceramics prepared in this work by mechanosynthesis with ionic conductivity of other $LaAlO_3$-based ceramics reported in literature. The data on sintering conditions, relative density and activation energy of ionic conductivity are summarized in Table 5. While the preparation of lanthanum aluminate-based solid solutions was performed by variety of different techniques, sintering of dense aluminate ceramics still required high temperatures, and, in most cases, literature data on electrical transport properties are given for the samples with relative density ≤ 90%. Fig. 11 shows that ionic conductivity of mechanosynthesized $La_{0.85}Ca_{0.15}AlO_{3-\delta}$ at higher temperature, 900°C, is comparable to that of $LaAlO_3$-based materials with highest reported ionic transport. On the other hand, activation energy of ionic conductivity of ceramics prepared by mechanosynthesis is somewhat higher compared to the values reported in literature (Table 5).

Fig. 11

Table 5

As a result, $La_{0.85}Ca_{0.15}AlO_{3-\delta}$ ceramics exhibit a stronger drop of ionic conductivity with decreasing temperature. Apparently, this should be attributed to a significantly smaller grain size of ceramics prepared in this work due to employed preparation technique and lower sintering temperature. Submicron particle size results in a stronger contribution of grain boundaries to the total resistivity; as discussed above, at lower temperatures electrical properties are determined by grain boundary conductivity with higher activation energy. The follow up work is planned to include the optimization of mechanosynthesis parameters and sintering profile to suppress the grain boundary resistivity.

4. Conclusions

Ca-substituted $La_{1-x}Ca_xAlO_{3-\delta}$ (x = 0.05-0.20) perovskites were prepared by room-temperature mechanosynthesis technique. XRPD analyses showed formation of perovskite phase after 30 min of high-energy ball milling. Sintering at 1450°C yielded dense ceramics with relative density above 95%. Refinement of XRPD data revealed a decrease of lattice constant with increasing calcium content. XPS analysis confirmed incorporation of Ca cations into perovskite structure replacing La cations in their twelve-coordinated positions. FE-SEM/EDX investigations indicated homogeneity of the sintered samples with average cation composition very close to the nominal. Substitution by calcium was found to increase the total electrical conductivity by 2-3 orders of magnitude compared to undoped $LaAlO_3$ in air. In $La_{1-x}Ca_xAlO_{3-\delta}$ (x = 0.05-0.20) series, partial oxygen-ionic conductivity increases with increasing calcium content up to 10 at.% in the lanthanum sublattice and is nearly independent of composition on further substitution, while p-type electronic conductivity tends to decrease slightly with x. All studied $La_{1-x}Ca_xAlO_{3-\delta}$ ceramics are mixed ionic-electronic conductors under oxidizing conditions. Oxygen-ionic contribution to the total conductivity increases with Ca content, with temperature and with reducing oxygen partial pressure. Under reducing conditions, when $p(O_2)$ is below 10^{-12}-10^{-10} atm, $La_{1-x}Ca_xAlO_{3-\delta}$ (x = 0.05-0.20) perovskites are oxygen-ionic conductors with negligible contribution of electronic transport. Average submicron grain size of mechanosynthesized $La_{1-x}Ca_xAlO_{3-\delta}$ ceramics results, however, in a prevailing contribution of grain boundaries to the total resistivity at temperatures below approximately 800°C.

References

1. K.Z. Fung, T.Y. Chen, Cathode-supported SOFC using a highly conductive lanthanum aluminate-based electrolyte, Solid State Ion. 188 (2011) 64–68. https://doi.org/10.1016/j.ssi.2010.09.035.

2. T. Takahashi, H. Iwahara, Ionic conduction in perovskite-type oxide solid solution and its application to the solid electrolyte fuel cell, Energy Conversion. 11 (1971) 105–111. https://doi.org/10.1016/0013-7480(71)90121-5.

3. C.A. da Silva, P.E.V. de Miranda, Synthesis of $LaAlO_3$ based materials for potential use as methane-fueled solid oxide fuel cell anodes, Int. J. Hydrogen Energy 40 (2015) 10002–10015. https://doi.org/10.1016/j.ijhydene.2015.06.019.

4. T.Y. Chen, K.Z. Fung, Comparison of dissolution behavior and ionic conduction between Sr and/or Mg doped $LaGaO_3$ and $LaAlO_3$, J. Power Sources 132 (2004) 1–10. https://doi.org/10.1016/j.jpowsour.2003.12.062.

5. J.A. Kilner, P. Barrow, R.J. Brook, M.J. Norgett, Electrolytes for the high temperature fuel cell; experimental and theoretical studies of the perovskite $LaAlO_3$, J. Power Sources 3 (1978) 67–80. https://doi.org./10.1016/0378-7753(78)80006-8.

6. T. Ishihara, H. Matsuda, Y. Takita, Oxide ion conductivity in doped $NdAlO_3$ perovskite-type oxides, J. Electrochem. Soc. 141 (1994) 3444–3449. https://doi.org/10.1149/1.2059351.

7. H. Matsuda, T. Ishihara, Y. Mizuhara, Y. Takita, Oxygen ion conductivity of doped $LnAlO_3$ perovskite oxide. Proceedings of The Electrochemical Society, PV 4 (1993) 129–136. https://doi.org/10.1149/199304.0129PV.

8. K.W. Browall, O. Muller, R.H. Doremus, Oxygen ion conductivity in oxygen-deficient perovskite-related oxides, Mater. Res. Bull. 11 (1976) 1475–1481. https://doi.org/10.1016/0025-5408(76)90097-0.

9. P.S. Anderson, G.C. Mather, F.M.B. Marques, D.C. Sinclair, A.R. West, Synthesis and characterization of $La_{0.95}Sr_{0.05}GaO_{3-\delta}$, $La_{0.95}Sr_{0.05}AlO_{3-\delta}$ and $Y_{0.95}Sr_{0.05}AlO_{3-\delta}$, J. Eur. Ceram. Soc. 19 (1999) 1665–1673. https://doi.org/10.1016/S0955-2219(98)00263-5.

10. T.L. Nguyen, M. Dokiya, S. Wang, H. Tagawa, T. Hashimoto, The effect of oxygen vacancy on the oxide ion mobility in $LaAlO_3$-based oxides, Solid State Ion. 130 (2000) 229–241. https://doi.org/10.1016/S0167-2738(00)00640-8.

11. D. Lybye, F.W. Poulsen, M. Mogensen, Conductivity of A- and B-site doped $LaAlO_3$, $LaGaO_3$, $LaScO_3$ and $LaInO_3$ perovskites, Solid State Ion. 128 (2000) 91–103. https://doi.org/10.1016/S0167-2738(99)00337-9.

12. J.Y. Park, G.M. Choi, Electrical conductivity of Sr and Mg doped $LaAlO_3$, Solid State Ion. 154–155 (2002) 535–540. https://doi.org/10.1016/S0167-2738(02)00510-6.

13. K. Nomura, S. Tanase, Electrical conduction behavior in $(La_{0.9}Sr_{0.1})M^{III}O_{3-\delta}$ (M^{III} = Al, Ga, Sc, In, and Lu) perovskites, Solid State Ionics 98 (1997) 229–236. https://doi.org/10.1016/S0167-2738(97)00101-X.

14. Q.X. Fu, F. Tietz, P. Lersch, D. Stöver, Evaluation of Sr- and Mn-substituted $LaAlO_3$ as potential SOFC anode materials, Solid State Ion. 177 (2006) 1059–1069. https://doi.org./10.1016/j.ssi.2006.02.053.

15. Q. Fu, F. Tietz, D. Stöver, Synthesis and electrical conductivity of Sr- and Mn-substituted $LaAlO_3$ as a possible anode material, Solid State Ion. 177 (2006) 1819–1822. https://doi.org/10.1016/j.ssi.2006.03.028.

16. L.A. Villas-Boas, D.P.F. de Souza, The effect of Pr co-doping on the densification and electrical properties of Sr-$LaAlO_3$, Mat. Res. 16 (2013) 982–989. http://dx.doi.org/10.1590/S1516-14392013005000087.

17. E.V. Tsipis, V.V. Kharton, Electrode materials and reaction mechanisms in solid oxide fuel cells: a brief review. I. Performance-determining factors, J. Solid State Electrochem. 12 (2008) 1039–1060. https://doi.org/10.1007/s10008-007-0468-0.

18. I. Yasuda, Y. Matsuzaki, T. Yamakawa, T. Koyama, Electrical conductivity and mechanical properties of alumina-dispersed doped lanthanum gallates, Solid State Ionics 135 (2000) 381-388. https://doi.org/10.1016/S0167-2738(00)00473-2.

19. T.L. Nguyen, M. Dokiya, Electrical conductivity, thermal expansion and reaction of $(La,Sr)(Ga,Mg)O_3$ and $(La,Sr)AlO_3$ system, Solid State Ionics 132 (2000) 217-226. https://doi.org/10.1016/S0167-2738(00)00661-5.

20. W. Araki, K. Takeda, Y. Arai, Mechanical behaviour of ferroelastic lanthanum metal oxides $LaMO_3$ (M=Co, Al, Ga, Fe), J. Eur. Ceram. Soc. 36 (2016) 4089–4094. https://doi.org/10.1016/j.jeurceramsoc.2016.07.006.

21. P.S. Anderson, F.M.B. Marques, D.C. Sinclair, A.R. West, Ionic and electronic conduction in $La_{0.95}Sr_{0.05}GaO_{3-\delta}$, $La_{0.95}Sr_{0.05}AlO_{3-\delta}$ and $Y_{0.95}Sr_{0.05}AlO_{3-\delta}$, Solid State Ion. 118 (1999) 229–239. https://doi.org/10.1016/S0167-2738(98)00465-2.

22. M.N. Danchevskaya, Y.D. Ivakin, S.N. Torbin, G.P. Muravieva, O.G. Ovchinnikova, Thermovaporous synthesis of complicated oxides, J. Mater. Sci. 41 (2006) 1385–1390. https://doi.org/10.1007/s10853-006-7411-0.

23. J. Chandradass, K.H. Kim, Synthesis and characterization of $LaAlO_3$ nanopowders by emulsion combustin method, J. Alloys Compd. 481 (2009) L31–L34. https://doi.org/10.1016/j.jallcom.2009.03.072.

24. J. Chandradass, K.H. Kim, Mixture of fuels approach for the solution combustion synthesis of $LaAlO_3$ nanopowders, Adv. Powder Technol. 21 (2010) 100–105. https://doi.org/10.1016/j.apt.2009.10.014.

25. M.D.S. Kumar, T.M. Srinivasan, P. Ramasamy, C. Subramanian, Synthesis of lanthanum aluminate by a citrate-combustion route, Mater. Lett. 25 (1995) 171–174. https://doi.org/10.1016/0167-577X(95)00149-2.

26. Z.Q. Tian, H.T. Yu, Z.L. Wang, Combustion synthesis and characterization of nanocrystalline $LaAlO_3$ powders, Mater. Chem. Phys. 106 (2007) 126–129. https://doi.org/10.1016/j.matchemphys.2007.05.027.

27. J. Chandradass, K.H. Kim, Size-controlled synthesis of $LaAlO_3$ by reverse micelle method: Investigation of the effect of water-to-rutfactant ratio on the particle size, J Cryst. Growth 311 (2009) 3631–3635. https://doi.org/10.1016/j.jcrysgro.2009.06.012.
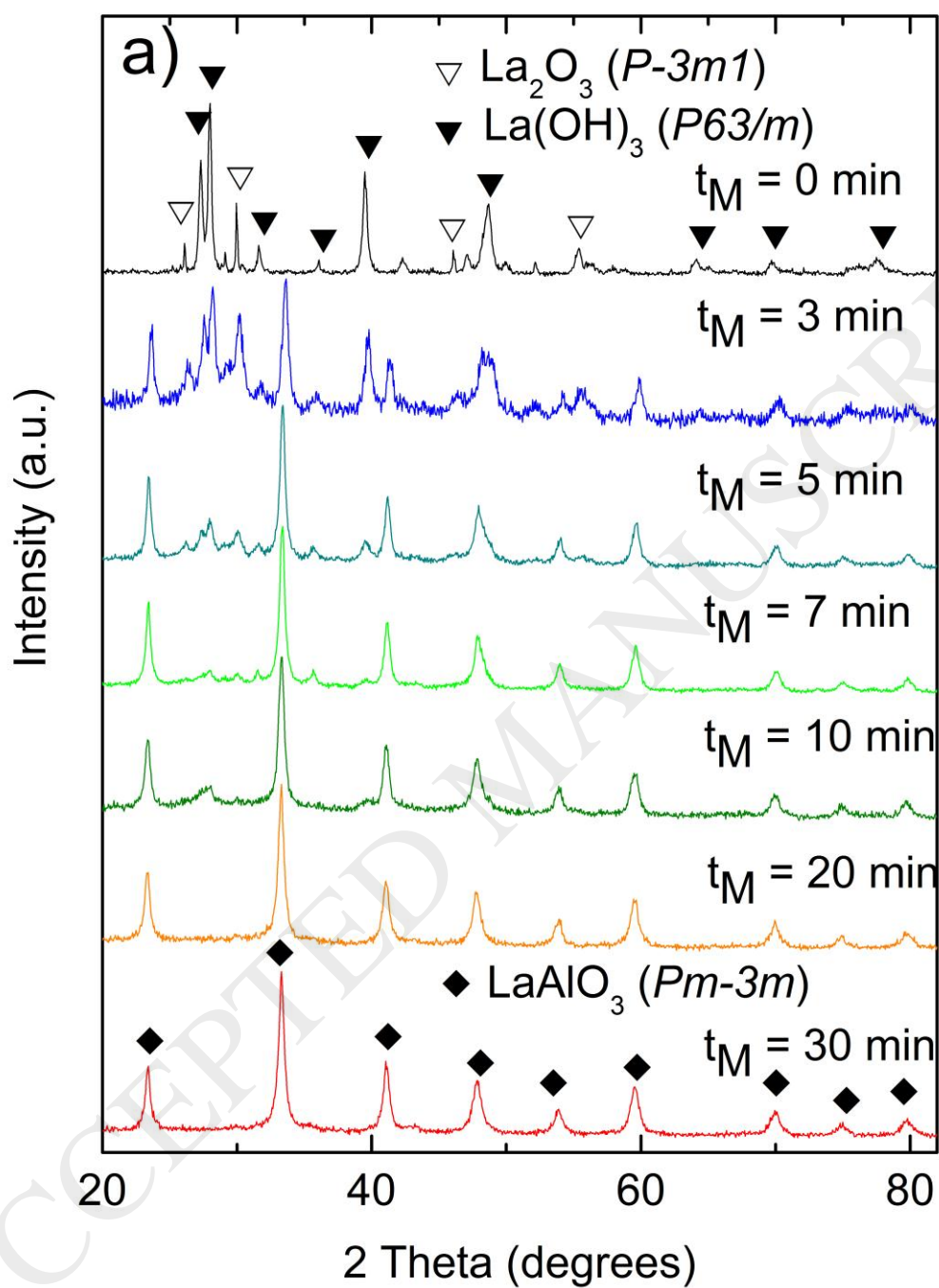
28. M. Kakihana, T. Okubo, Low temperature powder synthesis of $LaAlO_3$ through in situ polymerization route utilizing citric acid and ethylene glycol, J. Alloys Compd. 266 (1998) 129–133. https://doi.org/10.1016/S0925-8388(97)00445-3.

29. Z. Li, S. Zhang, W.E. Lee, Molten salt synthesis of $LaAlO_3$ powder at low temperatures, J. Eur. Ceram. Soc. 27 (2007) 3201–3205. https://doi.org/10.1016/j.jeurceramsoc.2007.01.008.

30. E. Mendoza-Mendoza, K.P. Padmasree, S.M. Montemayor, A.F. Fuentes, Molten salts synthesis and electrical properties of Sr-and/or Mg-doped perovskite-type $LaAlO_3$ powders, J. Mater. Sci. 47 (2012) 6076–6085. https://doi.org/10.1007/s10853-012-6520-1.

31. E. Taspinar, A.C. Tas, Low-temperature chemical synthesis of lanthanum monoaluminate, J. Am. Ceram. Soc. 80 (1997) 133–141. https://doi.org/10.1111/j.1151-2916.1997.tb02801.x.

32. G.H.A. Therese, M. Dinamani, P.V. Kamath, Electrochemical synthesis of perovskite oxides, J. Appl. Electrochem. 35 (2005) 459–465. https://doi.org/10.1007/s10800-004-8346-2.

33. Q. Zhang, F. Saito, Mechanochemical synthesis of lanthanum aluminate by grinding lanthanum oxide with transition alumina, J. Am. Ceram. Soc. 83 (2000) 439–441. https://doi.org/10.1111/j.1151-2916.2000.tb01215.x.

34. V. Šepelák, A. Düvel, M. Wilkening, K.D. Becker, P. Heitjans, Mechanochemical reactions and syntheses of oxides, Chem. Soc. Rev. 42 (2013) 7507–7520. https://doi.org/10.1039/C2CS35462D.

35. M.S. Islam, R.A. Davies, Atomistic study of dopant site-selectivity and defect association in the lanthanum gallate perovskite, J. Mater. Chem. 14 (2004) 86–93. https://doi.org/10.1039/B308519H.

36. A. Le Bail, H. Duroy, J.L. Fourquet, Ab-initio structure determination of $LiSbWO_6$ by X-ray powder diffraction, Mater. Res. Bull. 23 (1988) 447–452. https://doi.org/10.1016/0025-5408(88)90019-0.

37. J. Rodriguez-Carvajal, Fullprof Program, Version 2.4.2, ILL Grenoble, France, 1993.

38. P. Thompson, D.E. Cox, J.B. Hastings, Rietveld refinement of Debye-Scherrer synchrotron X-ray data from Al_2O_3, J. Appl. Crystallogr. 20 (1987) 79–83. https://doi.org/10.1107/S0021889887087090.

39. Joint Committee on Powder Diffraction, Standards (JCPDS) Powder Diffraction File (PDF), International Centre for Diffraction Data, Newtown Square, PA, 2004.

40. D. Shirley, High-resolution x-ray photoemission spectrum of the valence bands of gold, Phys. Rev. B 5 (1972) 4709–4714. https://doi.org/10.1103/PhysRevB.5.4709.

41. J.H. Scofield, Hartree-Slater subshell photoionization cross-sections at 1254 and 1487 eV, J. Electron. Spectrosc. Relat. Phenom. 8 (1976) 129–137. https://doi.org/10.1016/0368-2048(76)80015-1.

42. L. Samain, A. Jaworski, M. Edén, D.M. Ladd, D.K. Seo, F.J. Garcia-Garcia, U. Häussermann, Structural analysis of highly porous γ-Al_2O_3, J. Solid State Chem. 217 (2014) 1–8. https://doi.org/10.1016/j.jssc.2014.05.004.
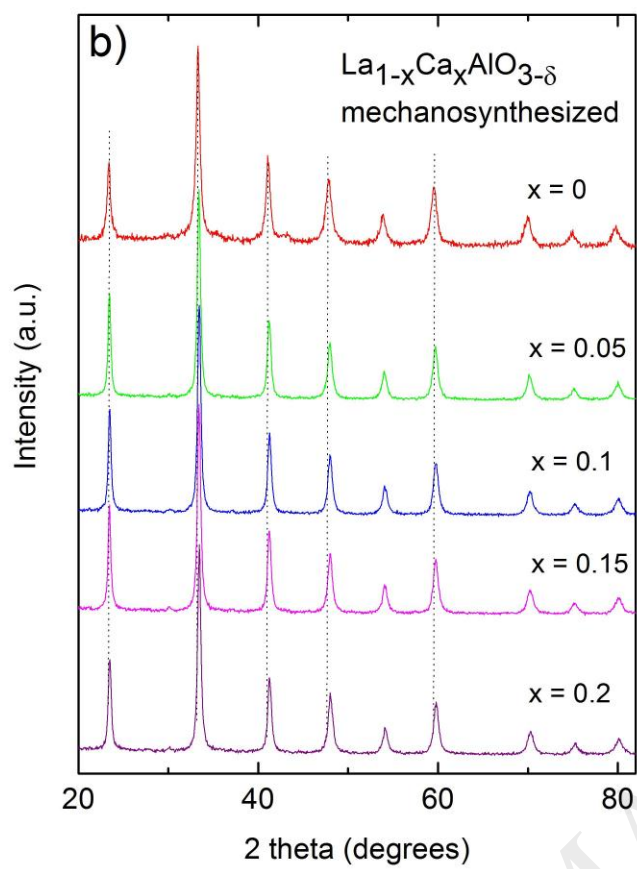
43. V.P. Gorelov, Transport number determinations in ionic conductors using EMF measurements with active load, Sov. Electrochem. 24 (1988) 272–274.

44. A.A. Yaremchenko, V.V. Kharton, E.N. Naumovich, F.M.B. Marques, Physicochemical and transport properties of BICUVOX-based ceramics, J. Electroceramics 4 (2000) 233–242. https://doi.org/10.1023/A:1009988531991.

45. V.V. Kharton, A.A. Yaremchenko, A.P. Viskup, G.C. Mather, E.N. Naumovich, F.M.B. Marques, Ionic and p-type electronic conduction in LaGa(Mg,Nb)O$_{3-\delta}$ perovskites, Solid State Ion. 128 (2000) 79–90. https://doi.org/10.1016/S0167-2738(99)00304-5.

46. C.A. Schneider, W.S. Rasband, K.W. Eliceri, NIH Image to ImageJ: 25 years of image analysis. Nat. Methods 9 (2012) 671–675. https://doi.org/10.1038/nmeth.2089.

47. R.D. Shannon, Revised effective ionic radii and systematic studies of interatomic distances in halides and chalcogenides, Acta Cryst. A 32 (1976) 751–767. https://doi.org/10.1107/S0567739476001551.

48. A. Nakatsuka, O. Ohtaka, H. Arima, N. Nakayama, T. Mizota, Cubic phase of single-crystal LaAlO$_3$ perovskite synthesized at 4.5 GPa and 1273 K, Acta Cryst. E 61 (2005) i148–i150. https://doi.org/10.1107/S1600536805020441.

49. M. Fabián, P. Bottke, V. Girman, A. Düvel, K.L. Da Silva, M. Wilkening, H. Hahn, P. Heitjans, V. Šepelák, A simple and straoghtforward mechanochemical synthesis of the far-from-equilibrium zinc aluminate ZnAl$_2$O$_4$ and its response to thermal treatment, RSC Adv. 5 (2015) 54321–54328. https://doi.org/10.1039/C5RA09098A.

50. G. Tyuliev, D. Panayotov, I. Avramova, D. Stoichev, T. Marinova, Thin-film coating of Cu-Co oxide catalyst on lanthana/zirconia films electrodeposited on stainless steel, Mater. Sci. Eng. C 23 (2003) 117–121. https://doi.org/10.1016/S0928-4931(02)00251-5.

51. K. Sood, K. Singh, S. Basu, O.P. Pandey, Preferential occupancy of Ca^{2+} dopant in La$_{1-x}$Ca$_x$InO$_{3-\delta}$ (x = 0–0.20) perovskite: structural and electrical properties, Ionics 21 (2015) 2839–2850. https://doi.org/10.1007/s11581-015-1461-8.

Figure captions

Fig. 1. a) XRPD patterns of the La_2O_3, $La(OH)_3$ and γ-Al_2O_3 mixture milled for various times (up to 30 min) illustrating the mechanochemical synthesis of the $LaAlO_3$; the milling times, t_M, are shown in the figure; b) XRPD patterns of mechanosynthesized $La_{1-x}Ca_xAlO_{3-\delta}$ (($0 \leq x \leq 0.2$)) solid solutions. Vertical lines represent a guide to eye to accent a shift of XRPD peaks due to the formation of the solid solution; c) XRPD patterns of sintered samples.
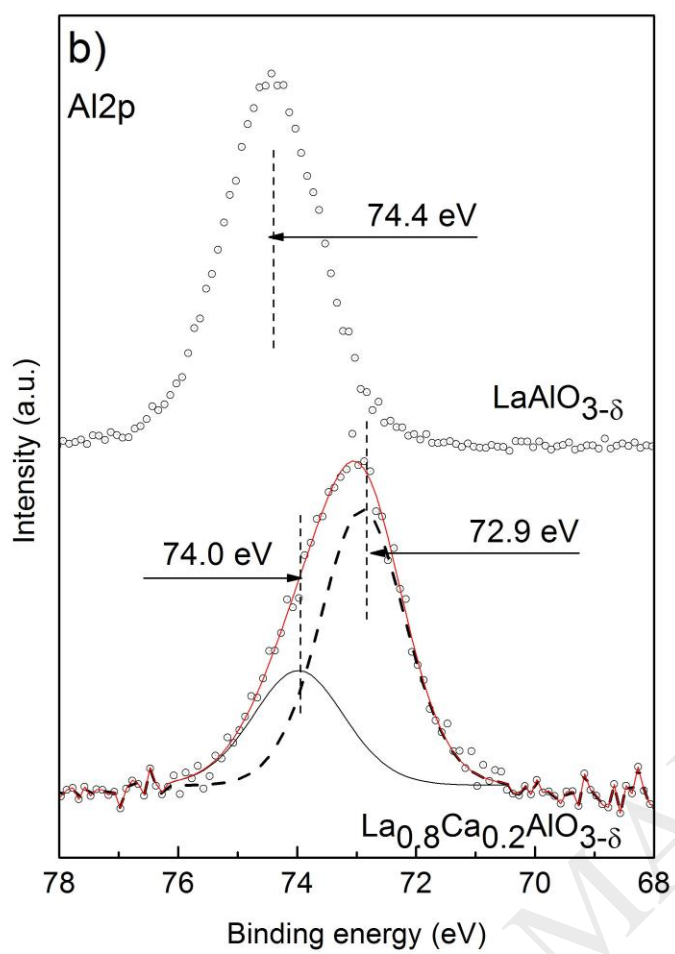
b)

$La_{1-x}Ca_xAlO_{3-\delta}$
mechanosynthesized

x = 0

x = 0.05

x = 0.1

x = 0.15

x = 0.2

Intensity (a.u.)

2 theta (degrees)
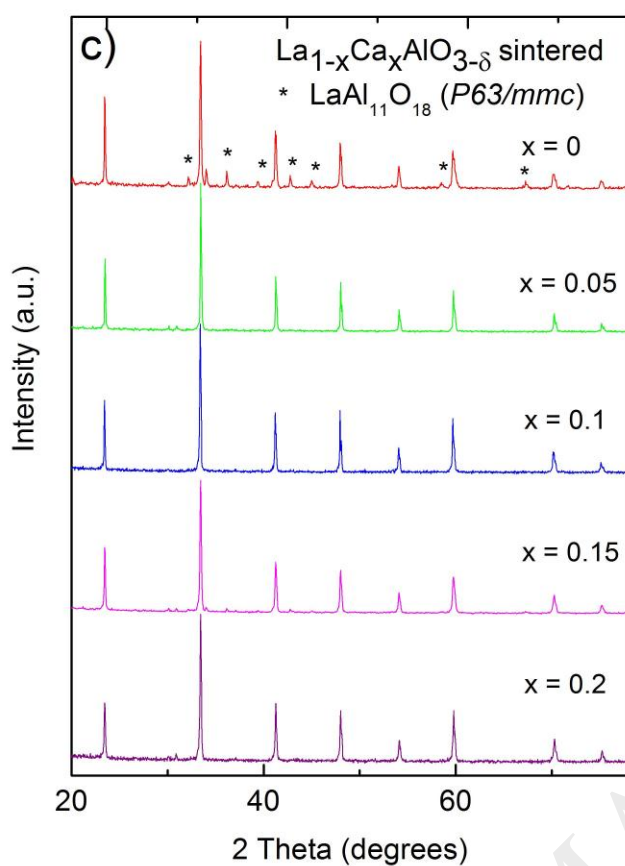
Fig. 2. XPS spectra of LaAlO$_3$ and La$_{0.8}$Ca$_{0.2}$AlO$_{3-\delta}$ ceramics: a) La3d$_{5/2}$ and its satellite; b) Al2p core level; c) Ca2p core level of La$_{0.8}$Ca$_{0.2}$AlO$_{3-\delta}$ compared with Ca2p core level of standard spectra measured for CaO (top) and CaTiO$_3$ (bottom).
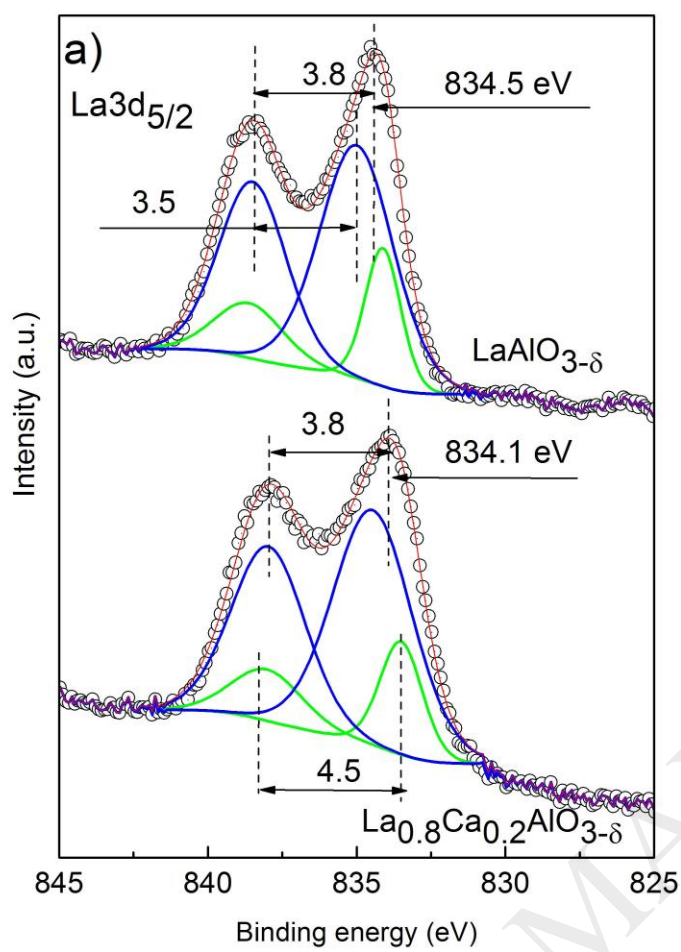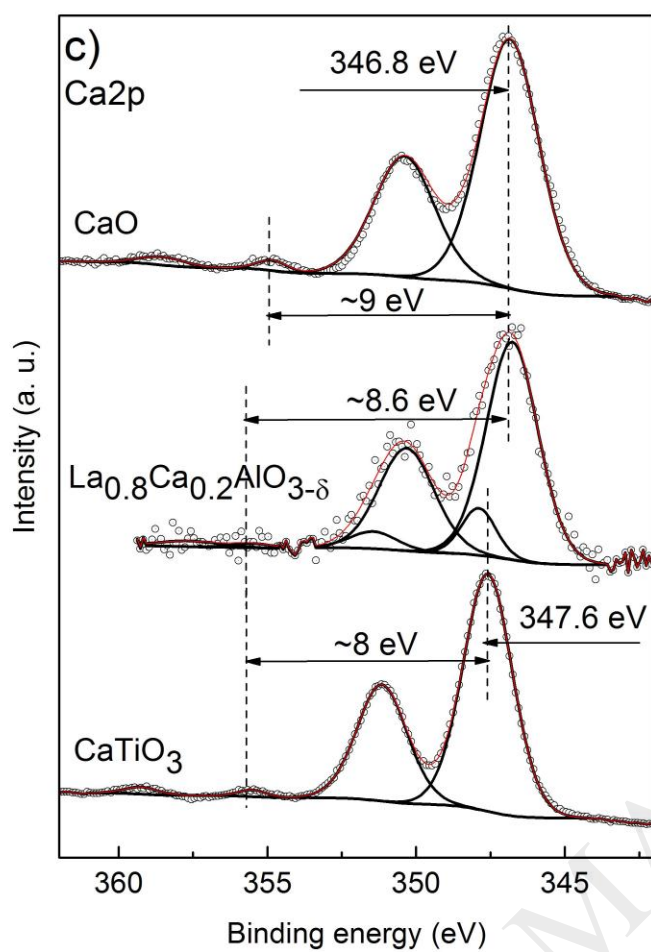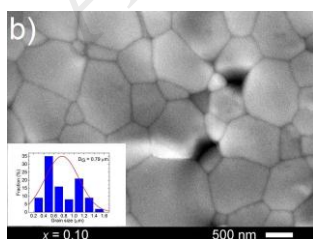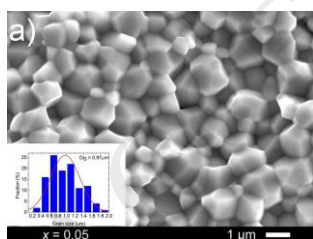
Fig. 3. SEM micrographs of fractured and thermally etched cross-sections of $La_{1-x}Ca_xAlO_{3-\delta}$ ceramics. a) $x = 0$; b) $x = 0.05$, c) $= 0.15$, d) $x = 0.15$, and e) elemental map of $La_{0.85}Ca_{0.15}AlO_{3-\delta}$. The insets show corresponding grain size distribution.

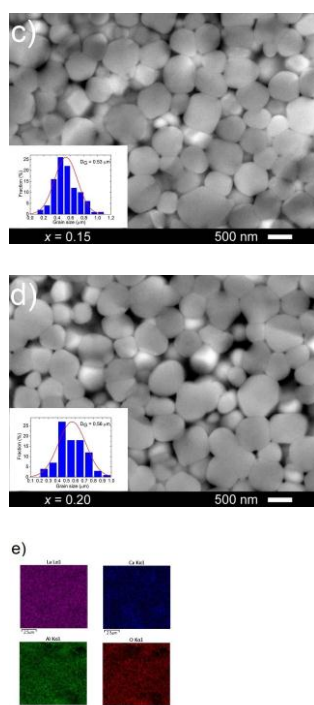Fig. 4. Temperature dependence of total electrical conductivity of La$_{1-x}$Ca$_x$AlO$_{3-\delta}$ ceramics in air.
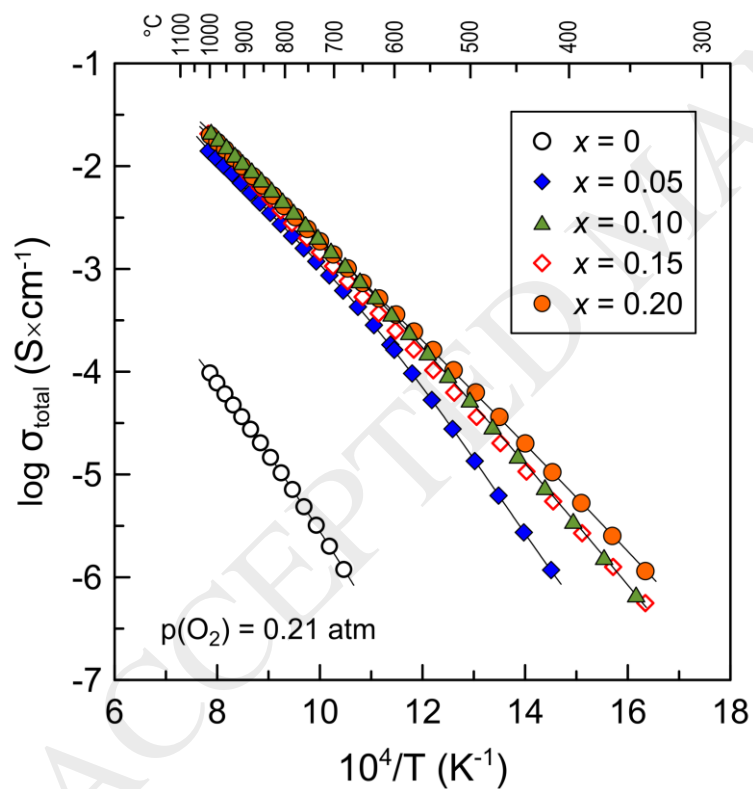

Fig. 5. Total electrical conductivity of La$_{1-x}$Ca$_x$AlO$_{3-\delta}$ ceramics in air as function of calcium content at 700-900°C.
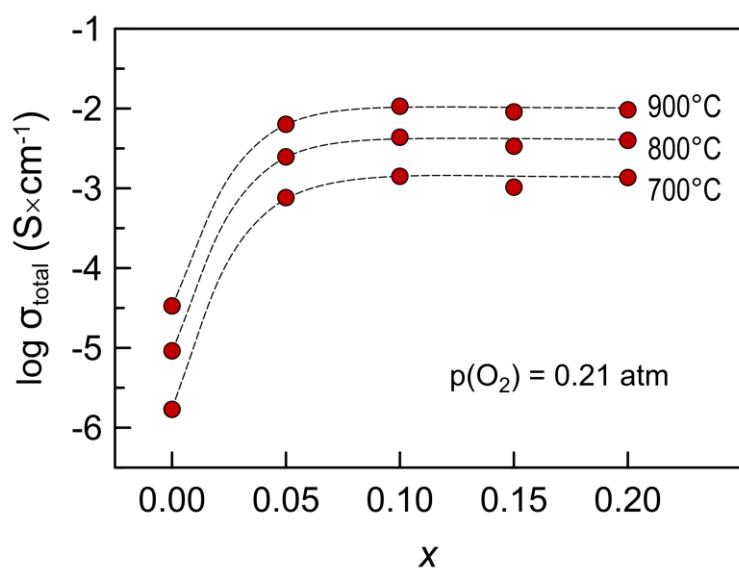
Fig. 6. Examples of the impedance spectra of $x = 0.15$ ceramics recorded in air at different temperatures. The spectra comprise the bulk contribution at high frequencies, the grain boundary contribution at intermediate frequencies, and low-frequency spike (at higher temperature) corresponding to the electrode polarization contribution.
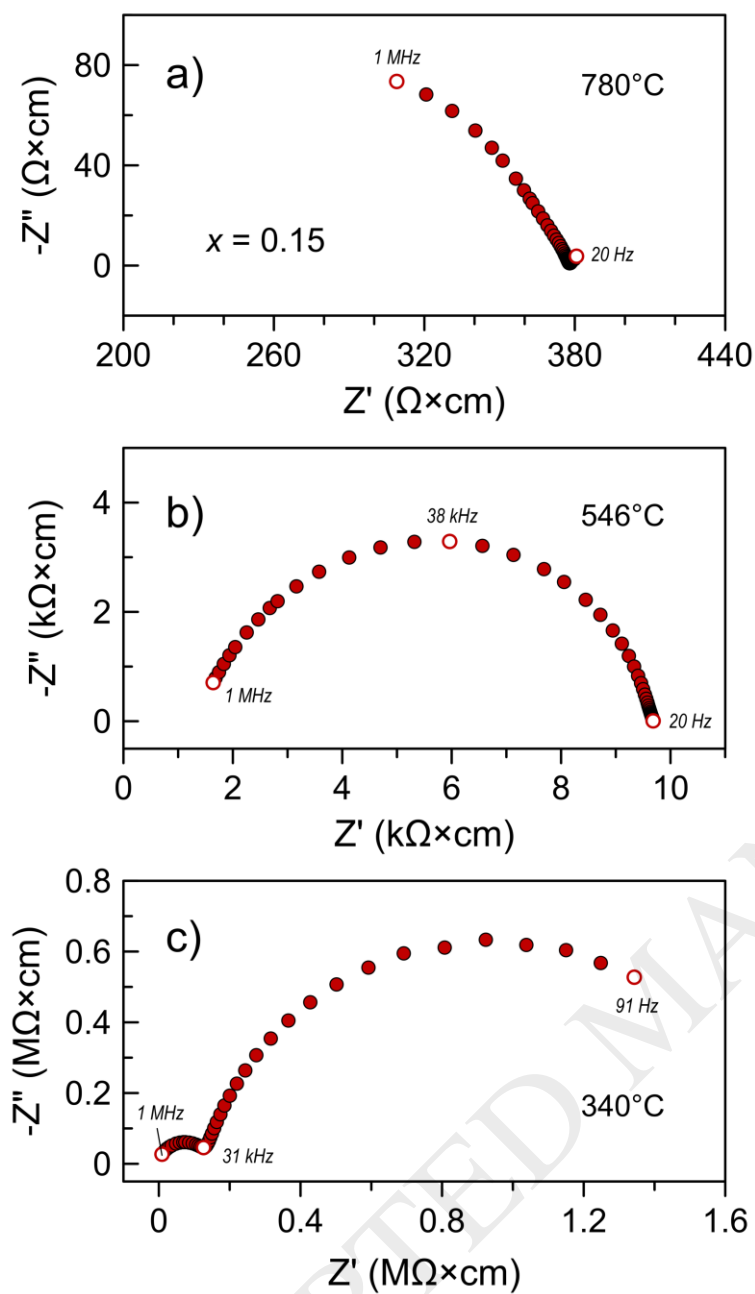
Fig. 7. (a) Temperature dependence of total, bulk and grain boundary conductivity of $x = 0.10$ ceramics in air; (b) Temperature dependence of bulk conductivity of $La_{1-x}Ca_xAlO_{3-\delta}$ ceramics in the low-temperature range in air. Dotted lines are an extrapolation to higher temperatures.

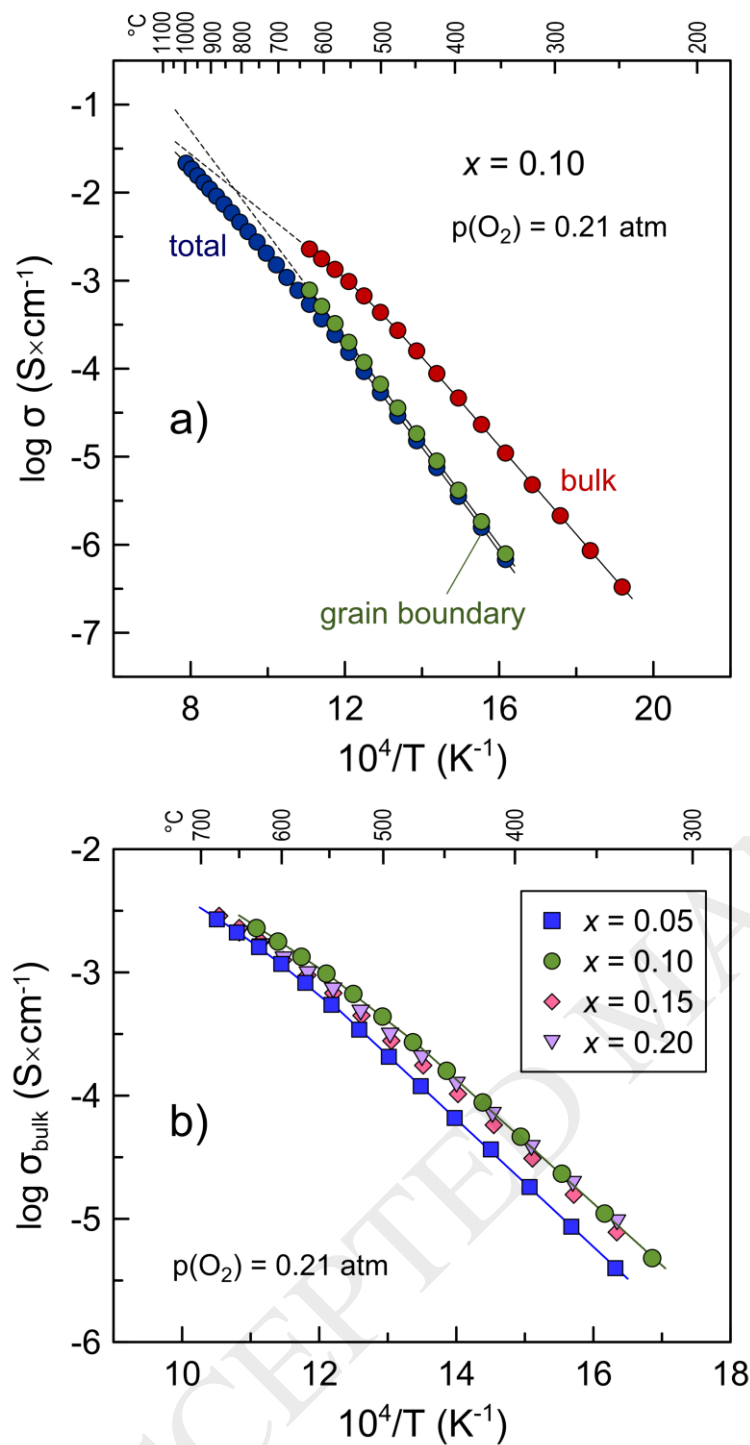Fig. 8. Oxygen partial pressure dependence of total electrical conductivity of (a) $La_{1-x}Ca_xAlO_{3-\delta}$ ceramics at 900°C, and (b) $La_{0.85}Ca_{0.15}AlO_{3-\delta}$ ceramics at 600-900°C; (c) experimental data points and calculated total and partial oxygen-ionic and p-type electronic conductivities for $x = 0.15$ at 800°C. All lines correspond to the fitting results using the model eqn.(7).
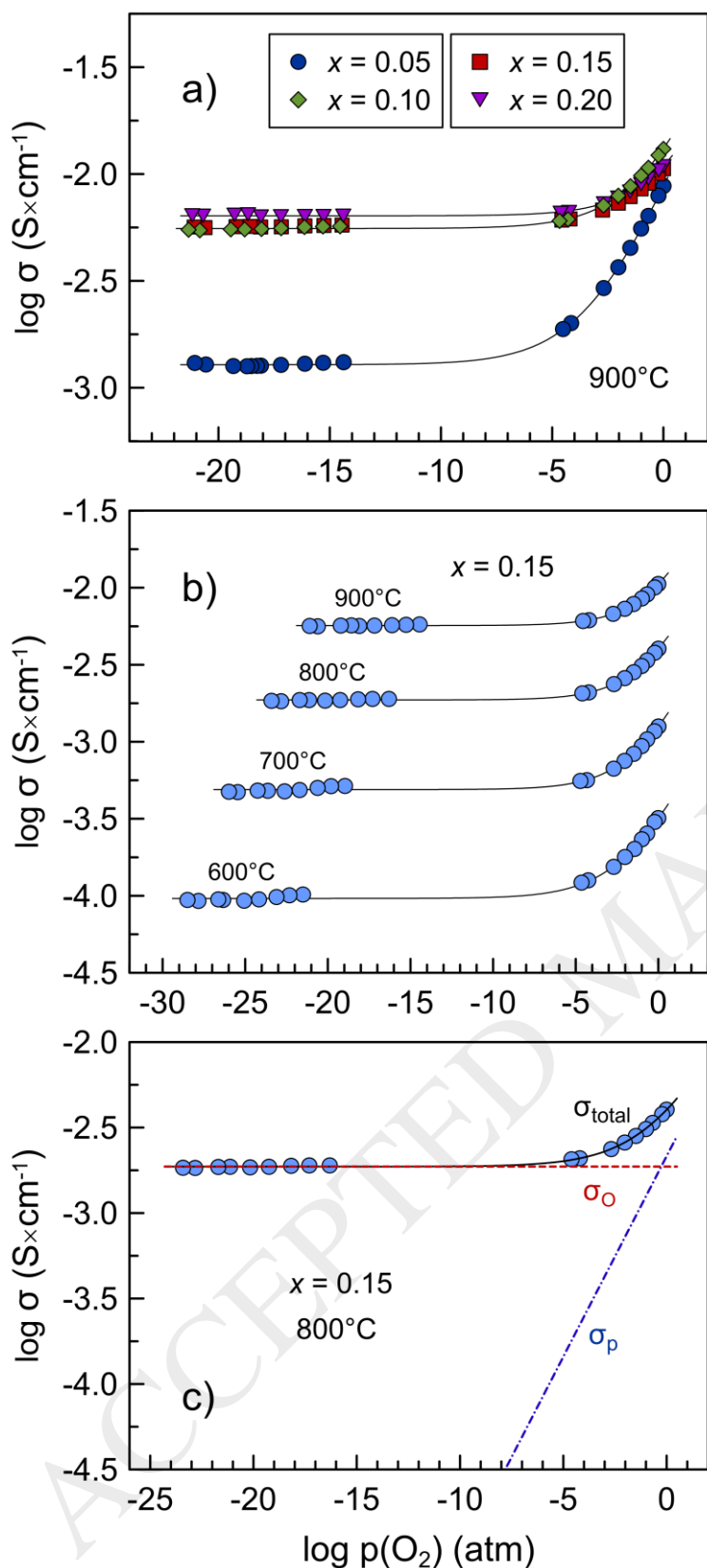
Fig. 9. (a) Variations of partial oxygen-ionic and *p*-type electronic conductivity of La$_{1-x}$Ca$_x$AlO$_{3-\delta}$ ceramics with calcium content at 900°C in air; (B) Arrhenius plot of total and partial ionic and electronic conductivity of *x* = 0.15 ceramics in air at 600-900°C. All values were obtained by fitting the p(O$_2$)-dependencies of total electrical conductivity using eqn.(7).
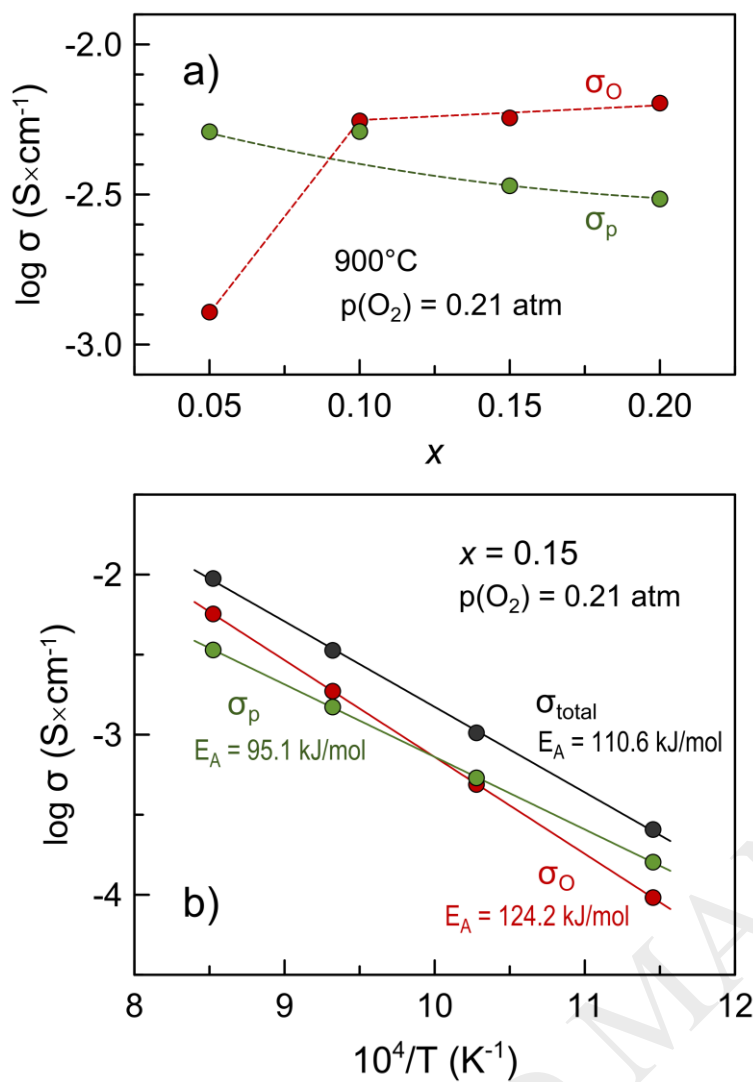
Fig. 10. Oxygen partial pressure dependence of oxygen-ion transference numbers of $La_{1-x}Ca_xAlO_{3-\delta}$ ceramics at 900°C calculated as $t_O = \sigma_O/\sigma_{total}$ from the results of fitting the σ vs $p(O_2)$ data using eqn.(7).

Fig. 11. Comparison of oxygen-ionic conductivity of mechanosynthesized $La_{0.85}Ca_{0.15}AlO_{3-\delta}$ with available literature data on $LaAlO_3$-based ceramics. Literature data are detailed in Table 5.
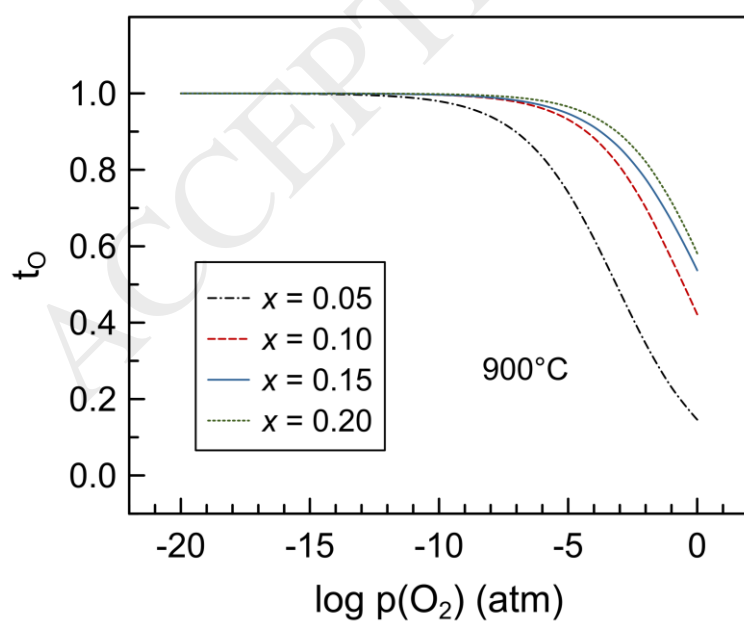
Table 1. Properties of as-mechanosynthesized and sintered $La_{1-x}Ca_xAlO_{3-\delta}$

as-prepared			
x	*Lattice parameter a, Å*	*Average crystallite size D, nm*	*Accumulated microstrain ($\times 10^{-4}$)*
0	3.8034(1)	11	19
0.05	3.7931(1)	30	39
0.10	3.7907(2)	33	52
0.15	3.7901(3)	39	57
0.20	3.7888(3)	34	70
sintered			
x	*Lattice parameter a, Å*	*Average grain size D_G, µm*	*Relative density, %*
0	3.7917(2)	1.18	62.7
0.05	3.7912(2)	0.97	96.7
0.10	3.7890(3)	0.79	96.1
0.15	3.7877(5)	0.53	95.3
0.20	3.7874(3)	0.56	96.5

Table 2. Elemental composition of $La_{1-x}Ca_xAlO_{3-\delta}$ samples determined by EDX analysis

Nominal elemental composition	Elemental composition determined by EDX
$LaAlO_3$	$LaAlO_3$
$La_{0.95}Ca_{0.05}AlO_{3-\delta}$	$La_{0.96}Ca_{0.04}AlO_{3-\delta}$
$La_{0.90}Ca_{0.10}AlO_{3-\delta}$	$La_{0.91}Ca_{0.09}AlO_{3-\delta}$
$La_{0.85}Ca_{0.15}AlO_{3-\delta}$	$La_{0.86}Ca_{0.14}AlO_{3-\delta}$
$La_{0.80}Ca_{0.20}AlO_{3-\delta}$	$La_{0.82}Ca_{0.18}AlO_{3-\delta}$

Table 3.Activation energy of the total electrical conductivity in air

X	T, °C	E_A, kJ/mol
0	680-1000	148.4 ± 1.0
0.05	630-1000	109.3 ± 0.4
	415-630	140.1 ± 0.9
0.10	630-1000	104.7 ± 0.4
	370-630	115.5 ± 0.5
0.15	340-1000	109.5 ± 0.2
0.20	340-1000	102.0 ± 0.3

Note: Activation energy was calculated using Arrhenius model $\sigma = (A_0 / T) \exp(-E_A /(RT))$; given errors are standard errors.

Table 4. Average oxygen-ion transference numbers determined by the modified EMF technique

x	T, °C	1.00 atm / 0.21 atm gradient	0.21 atm / p_1 gradient	
		$\overline{t_o}$	p_1, atm	$\overline{t_o}$
0.05	950	0.13 ± 0.01	7.0×10^{-17}	0.78 ± 0.01
	900	0.13 ± 0.01	7.7×10^{-18}	0.75 ± 0.01
	850		7.3×10^{-19}	0.74 ± 0.01
	800		1.0×10^{-19}	0.71 ± 0.01
	750		4.6×10^{-21}	0.69 ± 0.01
	700		2.7×10^{-22}	0.68 ± 0.01
0.10	900	0.40 ± 0.01	1.6×10^{-19}	0.892 ± 0.003
	850	0.41 ± 0.01	5.7×10^{-21}	0.918 ± 0.001
	800	0.39 ± 0.03	8.8×10^{-22}	0.925 ± 0.002
	750		3.6×10^{-23}	0.917 ± 0.002
	700		1.3×10^{-24}	0.922 ± 0.003
0.15	900	0.62 ± 0.01	5.7×10^{-20}	0.977 ± 0.001
	850	0.60 ± 0.01	6.2×10^{-21}	0.975 ± 0.001
	800	0.60 ± 0.01	1.7×10^{-22}	0.970 ± 0.001
	750	0.55 ± 0.01	2.2×10^{-23}	0.964 ± 0.001
	700	0.53 ± 0.01	4.7×10^{-25}	0.955 ± 0.001
0.20	900	0.60 ± 0.01	3.0×10^{-20}	0.994 ± 0.001
	850	0.56 ± 0.01	1.7×10^{-21}	0.995 ± 0.001
	800	0.55 ± 0.01	1.2×10^{-22}	0.993 ± 0.001
	750	0.53 ± 0.01	6.4×10^{-24}	0.995 ± 0.001
	700	0.47 ± 0.01	3.7×10^{-25}	0.991 ± 0.001

Note: given errors are the standard errors of regression model used in the modified EMF technique [43-45].

Table 5. Comparison of literature data for $LaAlO_3$-based ceramics

Composition	Sintering		Relative density, %	Activation energy for σ_O		Ref.
	T, °C	Time, h		T, °C	E_A, kJ/mol	
$La_{0.85}Ca_{0.15}AlO_{3-\delta}$	1450	12	95.3	600-900	124	this work
$La_{0.90}Ca_{0.10}AlO_{3-\delta}$	1600	12	-	725-970	106	[5]
$Nd_{0.90}Ca_{0.10}AlO_{3-\delta}$	1500	12	-	-	-	[6]
$Pr_{0.90}Ca_{0.10}AlO_{3-\delta}$	1650	-	87	-	-	[7]
$La_{0.95}Sr_{0.05}AlO_{3-\delta}$	1675	4	77	800-1000	111	[9,21]
$La_{0.90}Sr_{0.10}AlO_{3-\delta}$	1400<T<1600	4-7	72	750-900	110	[10]
$(La_{0.8}Sr_{0.2})_{0.94}AlO_{3-\delta}$	1500	10	90	410-910	107	[15]
$LaAl_{0.85}Mg_{0.15}O_{3-\delta}$	1950	0.25	-	1190-1280	95	[8]
$La_{0.90}Sr_{0.10}Al_{0.90}Mg_{0.10}O_{3-\delta}$ (*a*)	1650	4	98	800-1000	101	[12]
$La_{0.90}Sr_{0.10}Al_{0.90}Mg_{0.10}O_{3-\delta}$ (*b*)	1700	8	92.5	-	-	[11]

Note: Activation energy was calculated using Arrhenius model $\sigma = (A_0/T)\exp(-E_A/(RT))$.